

Determining interface structures in vertically aligned nanocomposite films

Bonan Zhu,^{1, a)} Georg Schusteritsch,^{1,2} Ping Lu,³ Judith L. MacManus-Driscoll,¹ and Chris J. Pickard^{1,2}

¹⁾*Department of Materials Science and Metallurgy, University of Cambridge*

²⁾*Advanced Institute for Materials Research, Tohoku University, 2-1-1 Katahira, Aoba, Sendai, 980-8577, Japan*

³⁾*Sandia National Laboratories, Albuquerque, New Mexico 87185, United States*

Vertically aligned nanocomposites (VANs) films have self-assembled pillar-matrix nanostructures. Owing to their large area-to-volume ratios, interfaces in VAN films are expected to play key roles in inducing functional properties, but our understanding is hindered by limited knowledge about their structures. Motivated by the lack of definitive explanation for the experimentally-found enhanced ionic conductivity in Sm-doped-CeO₂/SrTiO₃ VAN films, we determine the structure at vertical interfaces using random structure searching and explore how it can affect ionic conduction. Interatomic potentials are used to perform the initial searching, followed by first-principles calculations for refinement. Previously unknown structures are found, with lower energy than that of an optimized hand-built model. We find a strongly distorted oxygen sub-lattice which gives a complex landscape of vacancy energies. The cation lattice remains similar to the bulk phase, but has a localized strain field. The excess energy of the interface is similar to that of high angle grain boundaries in SrTiO₃.

^{a)}Electronic mail: bz240@cam.ac.uk

I. INTRODUCTION

Oxide thin films have a wide range of applications in electronic, magnetic and energy devices. Vertically aligned nanocomposite (VAN) films¹⁻³ are a new form of thin film material which contain nanopillars of one phase embedded in a matrix of another. Because of unique strain states, uniform strain, large area of interfaces, and perfectly clean interfaces in these structures⁴⁻⁷, they have been attracting a lot of interest for a wide range of functional systems^{3,8}. Also, VAN structures are easy to fabricate compared to planar superlattice films - they grow by self-assembly from a single target material using pulsed laser deposition, and the density of interfaces is very high with nanopillars of sizes around 10-20nm.

It is widely known that interfaces strongly influence mechanical, electrical and magnetic properties and also that at interfaces in planar heterostructures, novel functional properties often emerge⁹⁻¹¹. The local environment at an interface can be very different from that of the bulk material, which leads to reconstruction of the atomic and electronic structures. In VANs, the pillar-matrix nanostructure results in a large and thickness independent interface-to-volume ratio. The two phases with different structures are tightly coupled through these vertical interfaces. While theoretical and computational approaches are invaluable for studying interfaces, the atomic configurations need to be known to start with. Experimental determination of interface structures is very challenging. Although the advancement in scanning transmission electron microscopy (STEM) has allowed individual atomic columns to be imaged, determining the local structures often still requires extensive simulations and sometimes, intuition.

Recently, computational algorithms have been developed and enabled the prediction of structures for a range of materials¹²⁻¹⁵. Ab-initio random structure searching (AIRSS) has been shown to successfully find stable structures for bulk crystals¹⁶⁻¹⁸, low dimensional structures¹⁹, point defects^{20,21}, and interfaces²². Other search methods, such as those based on genetic algorithms and Bayesian optimisations, have also been reported to address structures at grain boundaries²³⁻²⁶ and heterostructures^{27,28}.

In this work, we study the interfaces in VAN films consisting of Sm-doped-CeO₂(20 at.%) pillars embedded in a matrix of SrTiO₃ (STO). Sm-doped-CeO₂ has a fluorite structure and is an ionic conductor²⁹, while STO has a perovskite structure and is insulating. The former undergoes a 45-degree rotation when epitaxially grown on STO substrates such that its [110]

direction is aligned with the [100] direction of STO. A schematic of the nanostructure and crystallographic directions is shown in Figure 1d. This system and similar ones have been reported to give enhanced ionic conductivity along the out-of-plane direction^{6,30,31}, which makes them particularly attractive for micro solid oxide fuel cell applications. On the other hand, the roles of the vertical interfaces are still unclear. The effects of solid-solid interfaces on ionic conduction has been widely studied theoretically in planar heterostructures where the interface is between materials with the same structure^{32,33} or its effect is dominated by the strain^{34,35}. Only a few works directly addressed the interface structure^{27,28,36}. We are not aware of any atomic scale computational studies about the vertical interfaces in VAN films, to date. The mismatch in periodicity and the fact that two sides have different bulk structures make these interfaces rather complex. While the high crystallinity of the films (i.e. low defect concentration) has been suggested to be the key to the enhanced ionic conduction^{30,31}, the possibility that enhancements also occur along interfaces needs to be determined in a definitive way. Doing this experimentally is very difficult owing to the very small (sub-nm length scales) and low volumes of material involved in thin films and so theoretical approaches are very important to guide the understanding.

Using STEM images as the starting point, we determine the interface atomic configurations using random structure searching. A combination of interatomic potential and first-principles methods are used, which we will describe in the next section. We found previously unknown interface structures with lower energies than that of a locally optimized hand-built model. These structures share common motifs and have a highly distorted anion lattice. The implications of the findings in the context of local ionic conduction enhancement are discussed.

II. METHODS

A. Simulation details

We choose to focus on the interfaces formed between (100) and (110) planes of SrTiO₃ (STO) and Sm-doped-CeO₂ (SDC) as electron microscopy images show the majority of them are in this orientation. They are indicated with blue lines in Figure 1b. The image is captured with a scanning transmission electron microscope in high angle annular dark field mode.

The minor STO(110)/SDC(100) type interfaces are marked by green lines. The orientation, periodicity and alignment of atomic planes of the vertical interface can be inferred from the cross-sectional STEM image shown in Figure 1a. It appears that 7 unit cells of STO match to 5 unit cells of SDC in the [001] direction, as indicated by the arrows. Figure 1c shows matching of atomic planes at the vertical interface viewed along the [001] direction. We construct a schematic of the pillar-matrix nanostructure based on the images, which is shown in Figure 1d. Crystallographic directions and imaging planes of Figure 1a-c are labelled. Note that the STO matrix has the same orientation as the substrate.

As the starting point for structure searching, we construct an idealized interface model by joining the bulk structures. We limit ourselves to TiO₂ terminated STO as a faint line of Ti atoms can be identified between the two lattices, shown in Figure 1a with a dotted vertical line. The orientation relationship of the two sides is set to be consistent with plan view and cross-sectional STEM images as in Figure 1a&c. The experimental lattice constant of STO is 3.905 Å and that of CeO₂ is 5.41 Å. In the [001] direction, we match seven unit cells of STO to five unit cells of CeO₂. Two unit cells of STO along its [010] direction are included with matching units of CeO₂. We use the experimental lattice constant for STO and adjust that of CeO₂ to match in the interface plane. This means that CeO₂ is compressively strained by 2.0% along the STO[010] direction and tensile strained by 1.0% along the STO/CeO₂[001] direction. We do not expect the strain to significantly affect the interface structures. As a first approximation, we neglect the Sm dopants (20 at.%) in the structure searching and hence the problem becomes finding the stable interface structure between STO (100) and CeO₂ (110). Including dopants would significantly increase the search space of the interface structures. The cubic $Fm\bar{3}m$ phase of CeO₂ is stable at low-temperature in contrast to yttria-stabilized zirconia (YSZ) where the yttria dopant plays an important role in stabilizing the cubic phase.

Interfaces are inherently non-periodic along its normal direction. There are two schemes for embedding an interface in a periodic cell. A single interface can be formed by two slabs of the material, this composite slab is then separated from its periodic images by vacuum. To mimic bulk-like boundary conditions, we add extra bulk-like layers to the exposed surfaces. These layers are internally fixed but allowed to move as a whole. An alternative scheme is to construct a cell with two identical interfaces which are mirror images of each other. This is only possible because the bulk phases both have mirror planes parallel

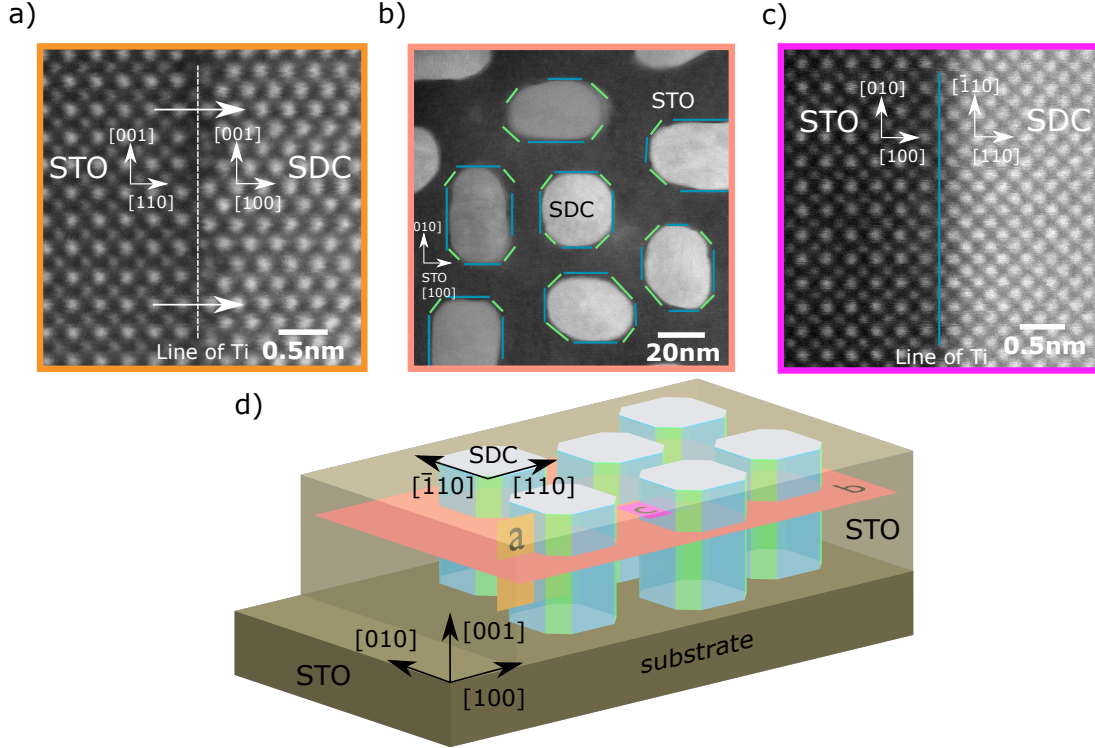


FIG. 1. a) A cross-sectional STEM high-angle annular dark-field (HAADF) image showing the STO(100)-SDC(110) interface viewed in the STO[010] direction. The two horizontal arrows mark the periodicity in the [001] direction. The vertical dashed line indicates the TiO_2 (100) termination plane of STO. b) A plan view STEM HAADF image showing bright SDC columns embedded in a darker STO matrix. The STO(100)-SDC(110) interface studied in this work is marked by the blue lines. The green lines mark the minor STO(110)-SDC(100) interfaces. c) A high magnification STEM HAADF image showing the STO-SDC vertical interface viewed along the [001] direction. The blue line marks the interface. d) A schematic of the VAN film structure. The SDC pillars are embedded in a matrix of STO with specific crystallographic matching. The image planes of a), b), and c) are labelled.

to the interface. Exposed surfaces are avoided at the price of almost doubling the number of atoms. Illustrations of the two schemes can be found in the supplementary material.

In-depth discussion of AIRSS³⁷ and how it can be applied to interface structure prediction has been described in previous work²². Here, we outline only the most relevant details in this study. AIRSS relies on generating random but physically sensible structures which are subsequently relaxed. To limit the search space, we choose species-pair dependent minimum

atomic separation constraints based on the values in bulk STO and CeO₂. We also choose the randomized region to be within 1 or 2 atomic layers from the interface, which will be discussed later. Instead of full randomization, we displace atoms randomly from their positions in the idealized model. This avoids forming clusters of similarly charged ions, which otherwise can give rise to high electrostatic energies. Maximum displacement magnitudes of 4 Å and 2 Å are used in lateral and normal directions to the interface respectively. Random structures generated with these parameters no longer have the preexisting order at the interface as in the initial model. Periodic cells with two identical interfaces are used for searching using interatomic potentials. Selected low energy structures are converted into slab models that each includes a single interface for further DFT calculations. More details can be found in the supplementary material.

DFT calculations are exceedingly expensive to use for structure searching of systems that contain as many atoms as the interfaces require here, since even a minimal cell in the slab geometry including 4 atomic layers for each side already has 260 atoms. Hence, we choose to use empirical interatomic potentials for searching, followed by refinement DFT calculations. Buckingham potentials with long-range Coulomb interactions are used. For STO, we apply the same potentials which were used in previous structure searching works of STO grain boundaries²³ and ZrO₂-STO super-lattices^{27,28}. The potentials chosen for CeO₂ were previously used for studying dopant distribution and ionic transport near edge dislocations³⁸. Details of the potentials can be found in the supplementary material. The General Utility Lattice Program³⁹ (GULP) is used for relaxing random structures. The dual interface scheme described above is used. The cell size normal to the interface is allowed to relax.

Density functional theory calculations are performed using the plane-wave pseudopotential code CASTEP⁴⁰. Generalized gradient approximation based exchange-correlation functionals have been used in many other computational studies of STO and CeO₂ and were shown to give consistent results^{32,41–44}. PBEsol⁴⁵ is used here, since it gives lattice constants closer to the experimental values for both STO and CeO₂. The valence states $2s^2 2p^4$ for O, the $3s^2 3p^6 3d^2 4s^2$ states for Ti, the $4s^2 4p^6 5s^2$ states for Sr and the $4f^1 5s^2 5p^6 5d^1 6s^2$ states for Ce are treated using on-the-fly generated core-corrected ultrasoft pseudopotentials. These pseudopotentials are soft and allow a plane wave cut off energy of 350 eV to be used. Their generation settings are tabulated in the supplementary material. A Monkhorst-Pack

grid of $1 \times 4 \times 1$ is used for sampling the Brillouin Zone. We use the slab scheme described above to embed the interface in a periodic cell. The lattice constants are fixed during the geometry optimisation.

The Atomic Simulation Environment⁴⁶ (ASE) is used for setting up and manipulating structures. AiiDA⁴⁷ is used to prepare, submit and parse results for DFT calculations. To distinguish and classify the structures found, Smooth Overlap of Atomic Positions⁴⁸ (SOAP) implemented in the GAP suite⁴⁹ is used. More details are included in the supplementary material.

B. Experimental details

The Sm-doped-CeO₂/SrTiO₃ vertically aligned nanocomposite (VAN) film was prepared by pulsed-laser deposition (PLD) as described previously⁵⁰. An FEI TitanTM G2 80-200 scanning transmission electron microscope with a Cs probe corrector operated at 200 kV was used in this study. The STO/SDC interfaces were imaged by using a high-angle annular dark-field (HAADF) detector with a collection range of 60-160 mrad.

III. RESULTS AND DISCUSSION

We first check the effectiveness of our RSS approach by searching for the bulk structures of SrTiO₃ (STO) and CeO₂ using both DFT and interatomic potentials. An $I4/mcm$ phase of STO is found to have the lowest energy using DFT for relaxation which is consistent with the low temperature phase of STO found experimentally⁵¹. Using the interatomic potentials, the $Pm\bar{3}m$ cubic structure is found as the most stable one. The $Pm\bar{3}m$ phase is the high temperature phase and was found in the VAN films previously^{30,50}. For CeO₂, the $Fm\bar{3}m$ fluorite structure is the most stable one using both methods. These findings are consistent with experimental results⁵¹⁻⁵³ and existing structural prediction works^{22,23,27,28}.

Due to the large quantity of relaxed random structures, we choose to focus on structures that have low relative energies and can be found repetitively. The relative energy for each structure is defined as:

$$E_{rel} = E_{total} - E_{total}^{ref}, \tag{1}$$

where E_{total} is the total energy and E_{total}^{ref} is the total energy of the reference structure which

is chosen to be the structure with the lowest total energy. We note that the interatomic potentials can give additional local minima in its potential energy surface (PES) compared to DFT due to their fixed analytic form. Assuming a uniform sampling of the configuration space, the number of visits to the same minima is proportional to the hyper-volume of the basin it is in. These frequently visited minima are likely to represent basins that also exist in the real PES.

To check if the randomization zone is sufficiently large, we perform searches with one or two randomized atomic layers in each side of the interface. Having one extra layer shifts the distribution of the relative energies towards higher values with a broader spread. Most of the low energy structures can be found in both searches. Since none of the low energy structures is exclusively found with increased randomization zone size, we limit the number of randomized layers to be one on both sides in subsequent searches.

Due to the finite size of the search cells, interactions between an interface and its mirror images can affect the geometry optimized structures as well as their relative energies. To check the convergence of structures with respect to the number of layers included normal to the interface, we carry out searches with 4 to 10 layers. While up to 10 layers were required to converge relative energies between the unique structures, most of the structures can be found even with the lowest setting of 4 layers. This indicates interface self-interactions have a limited effect on the overall shape of the PES, despite the values of minima being shifted.

The five low energy structures found in this work are shown in Figure 2. The two lowest energy structures *A* and *B* are different in oxygen positions in the last SrO layer and each has a glide plane with space group *Pc*. A highly symmetric structure *C** is also found. It has a space group *Pmm2* and is 1.1 eV higher in energy in searches including 6 layers of material on each side. In fact, this structure can be obtained by a simple local optimization of the initial model structure. Two other structures *D* and *E* both lack any symmetry element. A common pattern emerges among these five structures as well as in many others that have low relative energies. In Figure 2, we fade out the regions where the atomic configurations are shared by different structures. This highlights where they differ from each other which is also where the oxygen sub-lattice is very different from the bulk phases.

Details of structure *A* are shown in Figure 3. The bulk structures of STO and CeO₂ are vastly different. In perovskite-structured STO, Ti atoms are six-fold coordinated by oxygen atoms in a vertex-sharing octahedron network. The Sr atoms are twelve-fold cuboctahedron

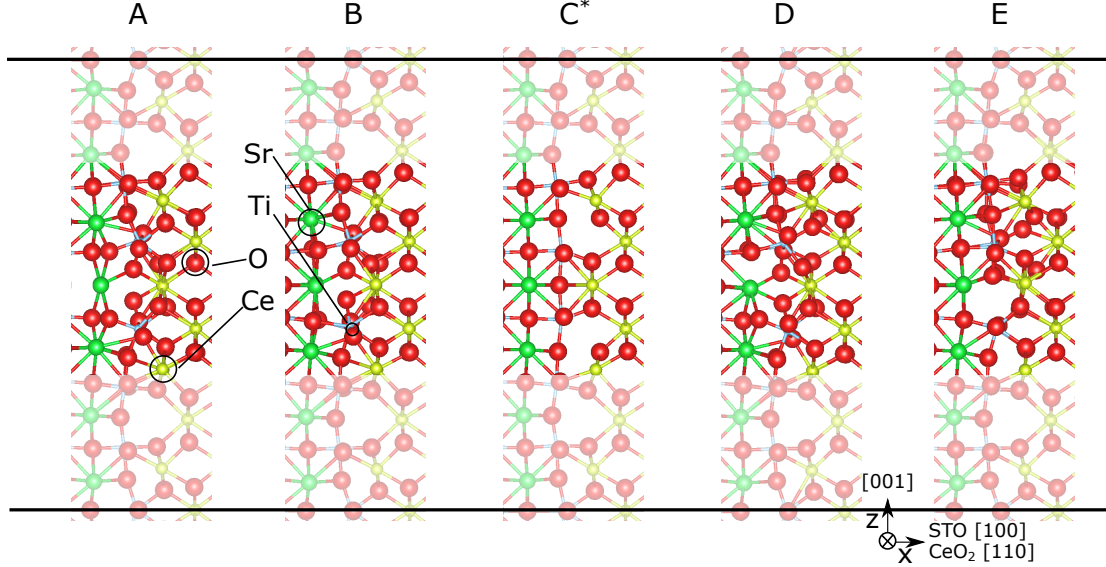


FIG. 2. Low energy structures found using the interatomic potentials, looking down the y (STO[010]) direction to show the atomic arrangements along z (STO[001]). We include only a small section of each simulation cell along x (STO[100]) to focus on the atomic configuration at the interfaces. The regions where atomic arrangement are shared are faded out in order to highlight the differences between these structures. Note that structure C^* is the result of a simple local optimization of the idealized model, and is also found during search.

coordinated, and each cuboctahedron shares faces with adjacent ones. In fluorite structured CeO_2 , Ce atoms are coordinated by eight oxygen atoms and coordination cubes share their edges. At the interface where 7 units cells of STO match to 5 unit cells of CeO_2 , the stacking sequence of STO (001) planes (i.e. $\text{SrO-TiO}_2\text{-SrO-TiO}_2$) and CeO_2 (110) planes (i.e. $\text{CeO}_2\text{-CeO}_2$) ends abruptly. If the sequences were not disrupted, 7 oxygen atoms would be placed in the next layer of the terminal TiO_2 plane, which continues the vertex-sharing Ti-O octahedron network. In reality, there are 10 oxygen atoms in the adjacent $\text{CeO}_2(001)$ plane. Similarly, it would have been 10 oxygen atoms in the next layer of the terminal CeO_2 plane, but only 7 adjacent oxygen atoms are present in the TiO_2 layer of STO (Figure 3b). Hence, the Ti atoms at the interface are over-coordinated and Ce atoms are under-coordinated. The latter is shown by the missing vertices of the Ce-O cube at the interface in Figure 3c. The mismatch of the bulk structure at the interface is mostly accommodated via the rearrangement of the oxygen sub-lattice, as highlighted by the rectangles in Figure 3ab. On the other hand, there is little distortion in the cation lattice at the interface, which

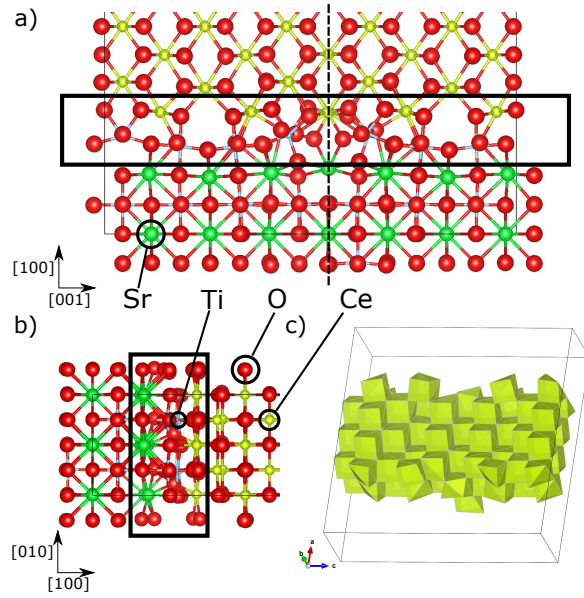


FIG. 3. Illustrations of Structure *A* that has the space group *Pc*. a) Viewing along the STO[010] direction. The glide plane is indicated by the dashed line. b) Viewing along the [001] direction. c) Distorted Ce-O₈ coordination polyhedron at the interface. Some of them have corners missing. Distortions of the Ti-O₆ octahedra are highlighted with rectangles in a) and b).

is consistent with the STEM images (shown in Figure 1abc), where visually there is little change of the atomic arrangement at the interfaces compared to the bulk. Note that the complex distortion of the anion lattice is missing in these images due to the relatively low atomic number of O atoms. This highlights the power of performing structure searching to reveal the full lattice information. The optimized initial model (structure *C**) has the space group *Pmm2*. Most of the structures found do not have any symmetry present at all, apart from a few at the low energy end of the distribution. Structure *A* has a glide plane parallel to the (001) planes with a translation of half of the lattice vector in STO[010] direction. This is marked by the dotted line in Figure 3a.

We next carry out DFT calculations on nine candidate structures and compare their relative energies with that given by the interatomic potentials. Our checks are limited to structures with six layers of materials on each side, due to the increasing computational costs with the cell size. In Figure 4, the energy differences per unit interface area ($\sigma^{rel} = E_{rel}/A_{itf}$) from DFT and interatomic potential calculations are plotted for comparison. In addition to the low energy structures, we include six structures with higher energy and label them

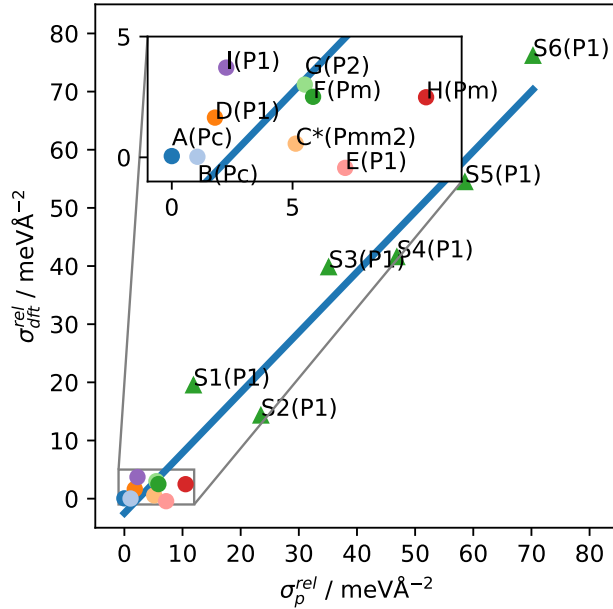


FIG. 4. Comparing the energy difference per unit area given by DFT (σ_{dft}^{rel}) and interatomic potentials (σ_p^{rel}). Structures are labeled by their name and symmetry. A positive correlation can be seen over the plotting range, indicated by the blue fitted line. On the other hand, there is little correlation when focused on the details over a small range, as shown in the inset.

as S1-6. A line is fitted to the data showing a positive correlation between the energies given by the two levels of theory over the plotting range. However, we find no correlation among the closely spaced low energy structures themselves, as shown in the inset of Figure 4. Structure E turns out to have the lowest energy given by DFT calculations, while it is $7 \text{ meV}\text{\AA}^{-2}$ higher in energy given by the interatomic potentials. In addition, *A* and *B* are two distinct structures found with the interatomic potentials, but they become the same after being optimized with DFT. It is known that empirical interatomic potentials can give more local minima. Ideally, we would like to search directly with DFT, but for a system as large as we consider here, it is prohibitively expensive to do so. The details of the PES are certainly different between these two levels of theory. Nevertheless, the trend over a relatively large energy range ($\approx 70 \text{ meV}\text{\AA}^{-2}$) is still captured by the interatomic potentials. The absence of correlations over a small energy range ($\approx 10 \text{ meV}\text{\AA}^{-2}$) means that it is necessary to refine a collection of structures with DFT calculations.

We compute the local strain for Ce atoms based on the averaged nearest neighbour

distances normalized by the mean value. The same is also done for STO using the Ti-Ti distances. In Figure 5b, each square represents a Ce column in structure E, and each triangle represents a Ti column, looking down the STO[010] direction. The sign of the strain alternates on each side of the interface going along the [001] direction. Tensile strained regions in CeO₂ are adjacent to compressively strained regions in STO. This strain field is quickly suppressed going into the bulk. Similar patterns also exist in other structures.

The interface can also influence the defect energy of oxygen vacancies. We calculate relative defect energies of oxygen vacancies in these structures using the interatomic potentials. A map of the relative formation energies in structure E is shown in Figure 5a. Here, oxygen sites are marked with circles, and the defect energy of bulk CeO₂ is chosen as the reference. All four atomic layers parallel to (010) planes of STO are included. The sizes of the circles are set according to their distances in the [010] direction, such that those further away appear smaller and may be overlapped by those in the front. A few sites at the interface have lower defect energy compared to that of the bulk, indicated by the dark green region in Figure 5a. We note that the existence of sites with very low defect energy suggests non-stoichiometric structures can become stable. However, it is challenging to perform the search with non-stoichiometric compositions since the interatomic potentials assume fixed ionic charges. The key point is that the mismatch in the crystal structure results in a complex energy landscape of the oxygen vacancies at the interface, which is likely to cause substantial trapping during vacancy migration.

We calculate the excess energy of the vertical interface using the approach of previous studies^{54,55}. More details can be found in the supplementary material. An excess energy of 0.91 J/m² is found for structure E. Note that the excess energies for STO symmetrical grain boundaries vary in a range of 0.5-1.5 J/m² depending on termination and orientation²²⁻²⁴. Despite significant structural mismatch, the vertical interface is energetically similar to the grain boundaries. The variations of excess energies among the low energy structures is on the order of 3 meV/Å² (0.05 J/m²). The small differences mean multiple configurations are accessible at elevated temperatures, resulting in a disordered anion lattice.

Misfit dislocations are important for heterogeneous interfaces in thin films as they allow the interface strain caused by the mismatch in the lattice constants to be relaxed. In the lattice match epitaxial growth model, the growth starts with one-to-one lattice mismatching, followed by dislocation formation at the film surface. The dislocations then glide down to

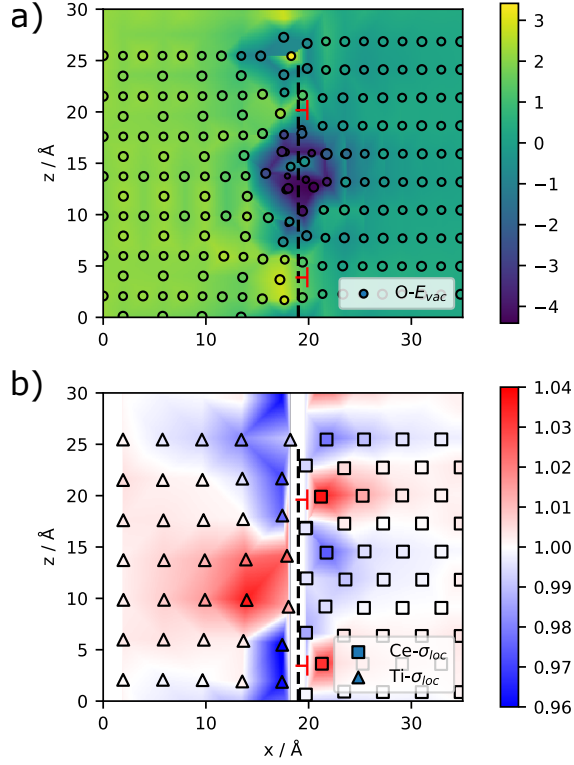


FIG. 5. a) Relative defect energies of oxygen vacancies mapped in the x - z plane for structure E, viewed in the same direction as that of Figure 2. The circles represent oxygen positions. The reference is set to the oxygen vacancy energy of bulk CeO_2 . b) Local strain of the Ce lattice in CeO_2 for the same view. Ce and Ti are labeled with squares and triangles respectively. The vacancy energy is related to the degree of distortion from the bulk lattice but not to the strain field. The two misfit dislocations are also marked in red at the interface.

the film-substrate interface. An extension of this model is domain matching epitaxy (DME) which applies when the mismatch in lattice parameter is so large that m lattice planes of one side are matched to n lattice planes of the other from the beginning of the growth⁵⁶, where both m and n are integers. In this work, 7 STO lattice planes match to 5 CeO_2 lattice planes along the $[001]$ direction. This can be regarded as alternating $3/2$ and $4/3$ matches between the two sides, which is consistent with the DME model. We identify two misfit dislocations at the vertical interface and indicate them in Figure 5. They are consistent with the localized strain field, where CeO_2 is tensile strained and STO is compressively strained in the vicinity of each. However, the strongest distortion of the oxygen sub-lattice does not take place at the

cores of dislocations, but is instead located in between them. In addition, the reduction of vacancy energy can be associated with the distortion of the anion lattice, as shown in Figure 5a, rather than located at the dislocation cores as reported in other studies^{38,57}. One possible cause of this is that the dislocations are closely spaced (16 Å). The strongly distorted anion lattice, as we have here, is not predicted under the framework of misfit dislocations based on lattice geometry. This highlights the advantage of doing systematic structure searching for understanding heterogeneous interfaces.

We now discuss the implications of the structures we found on the ionic conductivity at the vertical interfaces. First, we found a strain field highly localized at the interface, as shown in Figure 5. The effect of strain in fluorite structured ionic conductors has been studied in previous experimental and theoretical works^{31,34,35,58-60}. The ionic conductivity is expected to increase when the lattice is subject to tensile strain due to the decrease of the migration barrier. However, these results apply to uniform or gradually decaying strain field. The situation is different here as the strain field is localized and microscopic. Furthermore, Sun et al. showed, through molecular dynamics, that the strain field caused by dislocations leads to segregation of the dopant ions in doped ceria³⁸. Dopant ions often have different ionic radii compared to the Ce^{4+} ions, and by having them in the sites under local strain the elastic energy could be reduced. Both local enrichment and depletion of dopants are detrimental to the ionic conduction. The former increases the migration barrier as a result of stronger dopant-vacancy interactions, while the latter reduces the concentration of vacancies.

Second, by calculating the oxygen vacancy defect energies, sites with low relative defect energies are found at the interfaces. Once a vacancy diffuses into one of these sites, it is less likely to move out as the energy barrier of migration becomes much higher. As a result, the ionic conductivity is reduced locally. This is consistent with the work of Duholabhi et al.⁵⁷, where the diffusivity at the STO-MgO interface was calculated using the kinetic Monte-Carlo method. It was found that vacancy mobility was lowered due to trapping sites originating from the network of misfit dislocations at the interface.

Third, the DFT energies of the low-energy structures are found to be very closely spaced. This indicates that the interface is less likely to take a single structure under a finite temperature. Such structural degeneracy mostly takes place in the anion lattice. While a disordered anion sub-lattice could lead to an enhancement in ionic conductivity⁶¹, we note that for the

vertical interface this only takes place at the first interface layers of both sides. In addition, these disordered regions are confined, since they are separated by regions where atomic configurations are shared in many candidate structures, as illustrated in Figure 2. Hence, we do not expect this alone can enhance the ionic conductivity in the [001] direction.

In summary, we found a collection of lower energy structures of the STO(100)-CeO₂(110) vertical interfaces, including those with lower energies than that of the optimized hand-built model (C*, Figure 2). A highly distorted anion lattice was determined at these interfaces arising from the structural mismatch. The excess energies of interfaces are of the same order of magnitude as high angle grain boundaries in STO. We found interface misfit dislocation models are insufficient to describe the complex landscape of vacancy defect energies and the localized strain field in the structures.

IV. CONCLUSIONS

Random structure searching is used to determine interface configurations of the SrTiO₃(100)-CeO₂(110) vertical interface which forms naturally in vertically aligned nanocomposite (VAN) thin films. Lattice information in STEM images is used to constraint the search space to interface terminations and orientations that are physically present. We find previously unknown structures with energies lower than that of a locally relaxed model built by hand (C* Figure, 2). The interface excess energies of these structures are similar to that of high angle grain boundaries. We find a highly distorted oxygen anion lattices at the interfaces, while the cation lattice mostly remains similar to that of the bulk phases. The complex landscape of the defect energies is consistent with oxygen vacancies being trapped at the interface, rather than their mobility being enhanced. For the cation lattice, we find the strain field is non-uniform and is localized at the interface. Our findings provide a solid basis for further investigations on defect chemistry and migration of oxygen vacancies at the interface to reveal its effects on ionic conductivity. The structure searching approach can also be applied to other VAN systems showing a wide range of novel functionalities where the roles of vertical interfaces are not yet well understood.

V. SUPPLEMENTARY MATERIAL

See supplementary material for more details of the interatomic potentials, the pseudopotentials, interface structure searching and computing the excess energy.

ACKNOWLEDGMENTS

The calculations were performed on the CSD3 Supercomputer of the University of Cambridge (<http://www.hpc.cam.ac.uk/>), the Archer facility of the UK national high-performance computing service, and the UK Materials and Molecular Modelling Hub for which access was obtained via the UKCP consortium and funded by EPSRC grant No.EP/P022596/1. B.Z. acknowledges supports from the China Scholarship Council and the Cambridge Commonwealth, European and International Trust. J.L.M.D acknowledges supports by EPSRC grant No.EP/P007767/1. G.S. acknowledges supports from EPSRC grant No.EP/J010863/2. C.J.P. is supported by the Royal Society through a Royal Society Wolfson Research Merit award. Sandia National Laboratories is a multi-program laboratory managed and operated by National Technology and Engineering Solutions of Sandia, LLC., a wholly owned subsidiary of Honeywell International, Inc., for the U.S. Department of Energys National Nuclear Security Administration under contract DE-NA0003525.

We also thank Blas Uberuaga and Richard Hoagland at Los Alamos National Laboratory for fruitful discussions about the work.

REFERENCES

- ¹J. L. MacManus-Driscoll, “Self-Assembled Heteroepitaxial Oxide Nanocomposite Thin Film Structures: Designing Interface-Induced Functionality in Electronic Materials,” *Advanced Functional Materials* **20**, 2035–2045 (2010).
- ²J. L. MacManus-Driscoll, A. Suwardi, and H. Wang, “Composite epitaxial thin films: A new platform for tuning, probing, and exploiting mesoscale oxides,” *MRS BULLETIN* **40**, 933–942 (2015).
- ³J. Huang, J. L. MacManus-Driscoll, and H. Wang, “New epitaxy paradigm in epitaxial self-assembled oxide vertically aligned nanocomposite thin films,” *Journal of Materials Research* **32**, 4054–4066 (2017).

- ⁴J. L. MacManus-Driscoll, P. Zerrer, H. Wang, H. Yang, J. Yoon, A. Fouchet, R. Yu, M. G. Blamire, and Q. Jia, “Strain control and spontaneous phase ordering in vertical nanocomposite heteroepitaxial thin films,” *Nature Materials* **7**, 314–320 (2008).
- ⁵A. Chen, J.-M. Hu, P. Lu, T. Yang, W. Zhang, L. Li, T. Ahmed, E. Enriquez, M. Weigand, Q. Su, H. Wang, J.-X. Zhu, J. L. MacManus-Driscoll, L.-Q. Chen, D. Yarotski, and Q. Jia, “Role of scaffold network in controlling strain and functionalities of nanocomposite films,” *Science Advances* **2**, e1600245 (2016).
- ⁶S. Lee, W. Zhang, F. Khatkhatay, Q. Jia, H. Wang, and J. L. MacManus-Driscoll, “Strain Tuning and Strong Enhancement of Ionic Conductivity in SrZrO₃-RE₂O₃ (RE = Sm, Eu, Gd, Dy, and Er) Nanocomposite Films,” *ADVANCED FUNCTIONAL MATERIALS* **25**, 4328–4333 (2015).
- ⁷Q. Zhan, R. Yu, S. P. Crane, H. Zheng, C. Kisielowski, and R. Ramesh, “Structure and interface chemistry of perovskite-spinel nanocomposite thin films,” *Applied Physics Letters* **89**, 172902 (2006).
- ⁸W. Zhang, R. Ramesh, J. L. MacManus-Driscoll, and H. Wang, “Multifunctional, self-assembled oxide nanocomposite thin films and devices,” *MRS Bulletin* **40**, 736–745 (2015).
- ⁹A. Ohtomo and H. Y. Hwang, “A high-mobility electron gas at the LaAlO₃/SrTiO₃ heterointerface,” *Nature* **427**, 423–426 (2004).
- ¹⁰S. Okamoto and A. J. Millis, “Electronic reconstruction at an interface between a Mott insulator and a band insulator,” *Nature* **428**, 630–633 (2004).
- ¹¹P. Yu, J.-S. Lee, S. Okamoto, M. D. Rossell, M. Huijben, C.-H. Yang, Q. He, J. X. Zhang, S. Y. Yang, M. J. Lee, Q. M. Ramasse, R. Erni, Y.-H. Chu, D. A. Arena, C.-C. Kao, L. W. Martin, and R. Ramesh, “Interface Ferromagnetism and Orbital Reconstruction in BiFeO₃-La_{0.7}Sr_{0.3}MnO₃ Heterostructures,” *Physical Review Letters* **105**, 027201 (2010).
- ¹²C. J. Pickard and R. J. Needs, “High-Pressure Phases of Silane,” *Physical Review Letters* **97**, 045504 (2006).
- ¹³Y. Wang, J. Lv, L. Zhu, and Y. Ma, “Crystal structure prediction via particle-swarm optimization,” *Physical Review B* **82**, 094116 (2010).
- ¹⁴S. Goedecker, “Minima hopping: An efficient search method for the global minimum of the potential energy surface of complex molecular systems,” *The Journal of Chemical Physics* **120**, 9911–9917 (2004).

- ¹⁵A. R. Oganov, C. W. Glass, and S. Ono, “High-pressure phases of CaCO₃: Crystal structure prediction and experiment,” *Earth and Planetary Science Letters* **241**, 95–103 (2006).
- ¹⁶C. J. Pickard and R. J. Needs, “Structure of phase III of solid hydrogen,” *Nature Physics* **3**, 473–476 (2007).
- ¹⁷C. J. Pickard and R. J. Needs, “When is H₂O not water?” *The Journal of Chemical Physics* **127**, 244503 (2007).
- ¹⁸G. Schusteritsch, S. P. Hepplestone, and C. J. Pickard, “First-principles structure determination of interface materials: The NiInAs nickelides,” *Physical Review B - Condensed Matter and Materials Physics* **92**, 1–7 (2015).
- ¹⁹J. Chen, G. Schusteritsch, C. J. Pickard, C. G. Salzmann, and A. Michaelides, “Two Dimensional Ice from First Principles: Structures and Phase Transitions,” *Physical Review Letters* **116**, 025501 (2016), wOS:000368281600005.
- ²⁰A. J. Morris, C. J. Pickard, and R. J. Needs, “Hydrogen/silicon complexes in silicon from computational searches,” *Physical Review B* **78**, 184102 (2008).
- ²¹A. J. Morris, C. J. Pickard, and R. J. Needs, “Hydrogen/nitrogen/oxygen defect complexes in silicon from computational searches,” *Physical Review B* **80**, 144112 (2009).
- ²²G. Schusteritsch and C. J. Pickard, “Predicting interface structures: From SrTiO₃ to graphene,” *Physical Review B - Condensed Matter and Materials Physics* **90**, 1–7 (2014).
- ²³A. L.-S. Chua, N. A. Benedek, L. Chen, M. W. Finnis, and A. P. Sutton, “A genetic algorithm for predicting the structures of interfaces in multicomponent systems,” *Nature Materials* **9**, 418–422 (2010).
- ²⁴X. Zhao, Q. Shu, M. C. Nguyen, Y. Wang, M. Ji, H. Xiang, K.-M. Ho, X. Gong, and C.-Z. Wang, “Interface Structure Prediction from First-Principles,” *Journal of Physical Chemistry C* **118**, 9524–9530 (2014), wOS:000335878900025.
- ²⁵Q. Zhu, A. Samanta, B. Li, R. E. Rudd, and T. Frolov, “Predicting phase behavior of grain boundaries with evolutionary search and machine learning,” *Nature Communications* **9**, 467 (2018).
- ²⁶S. Kikuchi, H. Oda, S. Kiyohara, and T. Mizoguchi, “Bayesian optimization for efficient determination of metal oxide grain boundary structures,” *Physica B: Condensed Matter Special Issue on Frontiers in Materials Science: Condensed Matters*, **532**, 24–28 (2018).

- ²⁷W. L. Cheah and M. W. Finnis, “Structure of multilayer ZrO₂/SrTiO₃,” *Journal of Materials Science* **47**, 1631–1640 (2012), wOS:000299105200006.
- ²⁸W. L. Cheah, D. W. McComb, and M. W. Finnis, “Structure and ionic diffusivity in an yttria-stabilised zirconia/strontium titanate multilayer,” *Acta Materialia* **129**, 388–397 (2017).
- ²⁹H. Yahiro, Y. Eguchi, K. Eguchi, and H. Arai, “Oxygen ion conductivity of the ceria-samarium oxide system with fluorite structure,” *Journal of Applied Electrochemistry* **18**, 527–531 (1988).
- ³⁰S. M. Yang, S. Lee, J. Jian, W. Zhang, P. Lu, Q. Jia, H. Wang, T. W. Noh, S. V. Kalinin, and J. L. MacManus-Driscoll, “Strongly enhanced oxygen ion transport through samarium-doped CeO₂ nanopillars in nanocomposite films,” *NATURE COMMUNICATIONS* **6** (2015), 10.1038/ncomms9588.
- ³¹S. Lee, W. Zhang, F. Khatkhatay, H. Wang, Q. Jia, and J. L. MacManus-Driscoll, “Ionic Conductivity Increased by Two Orders of Magnitude in Micrometer-Thick Vertical Yttria-Stabilized ZrO₂ Nanocomposite Films.” *Nano letters* **15**, 7362–9 (2015).
- ³²D. S. Aidhy, B. Liu, Y. Zhang, and W. J. Weber, “Strain-Induced Phase and Oxygen-Vacancy Stability in Ionic Interfaces from First-Principles Calculations,” *Journal of Physical Chemistry C* **118**, 30139–30144 (2014), wOS:000347360200078.
- ³³D. S. Aidhy, Y. Zhang, and W. J. Weber, “Strained Ionic Interfaces: Effect on Oxygen Diffusivity from Atomistic Simulations,” *The Journal of Physical Chemistry C* **118**, 4207–4212 (2014).
- ³⁴R. A. D. Souza, A. Ramadan, and S. Hörner, “Modifying the barriers for oxygen-vacancy migration in fluorite-structured CeO₂ electrolytes through strain: A computer simulation study,” *Energy & Environmental Science* **5**, 5445–5453 (2012).
- ³⁵A. Kushima and B. Yildiz, “Oxygen ion diffusivity in strained yttria stabilized zirconia: Where is the fastest strain?” *Journal of Materials Chemistry* **20**, 4809–4809 (2010).
- ³⁶M. S. Dyer, G. R. Darling, J. B. Claridge, and M. J. Rosseinsky, “Chemical Bonding and Atomic Structure in Y₂O₃:ZrO₂-SrTiO₃ Layered Heterostructures,” *Angewandte Chemie International Edition* **51**, 3418–3422 (2012).
- ³⁷C. J. Pickard and R. J. Needs, “Ab initio random structure searching.” *Journal of physics. Condensed matter : an Institute of Physics journal* **23**, 053201–053201 (2011).

- ³⁸L. Sun, D. Marrocchelli, and B. Yildiz, “Edge dislocation slows down oxide ion diffusion in doped CeO₂ by segregation of charged defects,” *Nature Communications* **6**, ncomms7294 (2015).
- ³⁹J. D. Gale and A. L. Rohl, “The General Utility Lattice Program (GULP),” *Molecular Simulation* **29**, 291–341 (2003).
- ⁴⁰S. J. Clark, M. D. Segall, C. J. Pickard, P. J. Hasnip, M. I. J. Probert, K. Refson, and M. C. Payne, “First principles methods using CASTEP,” *Zeitschrift für Kristallographie* **220**, 567–570 (2005).
- ⁴¹Y. Choi, M. Scott, T. Söhnle, and H. Idriss, “A DFT + U computational study on stoichiometric and oxygen deficient M–CeO₂ systems (M = Pd1, Rh1, Rh10, Pd10 and Rh4Pd6),” *Physical Chemistry Chemical Physics* **16**, 22588–22599 (2014).
- ⁴²C. W. M. Castleton, J. Kullgren, and K. Hermansson, “Tuning LDA+U for electron localization and structure at oxygen vacancies in ceria,” *The Journal of Chemical Physics* **127**, 244704 (2007).
- ⁴³L. Triggiani, A. B. Muñoz-García, A. Agostiano, and M. Pavone, “Promoting oxygen vacancy formation and p-type conductivity in SrTiO₃ via alkali metal doping: A first principles study,” *Physical Chemistry Chemical Physics* **18**, 28951–28959 (2016).
- ⁴⁴R. Pentcheva and W. E. Pickett, “Avoiding the polarization catastrophe in LaAlO₃ overlayers on SrTiO₃(001) through polar distortion,” *Physical Review Letters* **102**, 3–6 (2009).
- ⁴⁵J. P. Perdew, A. Ruzsinszky, G. I. Csonka, O. A. Vydrov, G. E. Scuseria, L. A. Constantin, X. Zhou, and K. Burke, “Restoring the Density-Gradient Expansion for Exchange in Solids and Surfaces,” *Physical Review Letters* **100**, 136406 (2008).
- ⁴⁶A. H. Larsen, J. J. Mortensen, J. Blomqvist, I. E. Castelli, R. Christensen, Marcin Dulak, J. Friis, M. N. Groves, B. Hammer, C. Hargus, E. D. Hermes, P. C. Jennings, P. B. Jensen, J. Kermode, J. R. Kitchin, E. L. Kolsbjerg, J. Kubal, Kristen Kaasbjerg, S. Lysgaard, J. B. Maronsson, T. Maxson, T. Olsen, L. Pastewka, Andrew Peterson, C. Rostgaard, J. Schiøtz, O. Schütt, M. Strange, K. S. Thygesen, Tejs Vegge, L. Vilhelmsen, M. Walter, Z. Zeng, and K. W. Jacobsen, “The atomic simulation environment—a Python library for working with atoms,” *Journal of Physics: Condensed Matter* **29**, 273002 (2017).
- ⁴⁷G. Pizzi, A. Cepellotti, R. Sabatini, N. Marzari, and B. Kozinsky, “AiiDA: Automated interactive infrastructure and database for computational science,” *Computational Materials Science* **111**, 218–230 (2016).

- ⁴⁸A. P. Bartók, R. Kondor, and G. Csányi, “On representing chemical environments,” *Physical Review B* **87**, 184115 (2013).
- ⁴⁹A. P. Bartók, M. C. Payne, R. Kondor, and G. Csányi, “Gaussian Approximation Potentials: The Accuracy of Quantum Mechanics, without the Electrons,” *Physical Review Letters* **104**, 136403 (2010).
- ⁵⁰S. Cho, C. Yun, S. Tappertzhofen, A. Kursumovic, S. Lee, P. Lu, Q. Jia, M. Fan, J. Jian, H. Wang, S. Hofmann, and J. L. MacManus-Driscoll, “Self-assembled oxide films with tailored nanoscale ionic and electronic channels for controlled resistive switching,” *NATURE COMMUNICATIONS* **7** (2016), 10.1038/ncomms12373.
- ⁵¹K. Tsuda and M. Tanaka, “Refinement of crystal structure parameters using convergent-beam electron diffraction: The low-temperature phase of SrTiO₃,” *Acta Crystallographica Section A: Foundations of Crystallography* **51**, 7–19 (1995).
- ⁵²Y. A. Abramov, V. G. Tsirelson, V. E. Zavodnik, S. A. Ivanov, and I. D. Brown, “The chemical bond and atomic displacements in SrTiO₃ from X-ray diffraction analysis,” *Acta Crystallographica Section B: Structural Science* **51**, 942–951 (1995).
- ⁵³J. D. McCullough, “An X-Ray Study of the Rare-earth Oxide Systems: CeIV—NdIII, CrIV—PrIII, CeIV—PrIV and PrIV—NdIII1,” *Journal of the American Chemical Society* **72**, 1386–1390 (1950).
- ⁵⁴B. Feng, I. Sugiyama, H. Hojo, H. Ohta, N. Shibata, and Y. Ikuhara, “Atomic structures and oxygen dynamics of CeO₂ grain boundaries,” *Scientific Reports* **6**, 20288 (2016).
- ⁵⁵R. I. Eglitis and D. Vanderbilt, “First-principles calculations of atomic and electronic structure of SrTiO₃ (001) and (011) surfaces,” *Physical Review B* **77**, 195408 (2008).
- ⁵⁶J. Narayan and B. C. Larson, “Domain epitaxy: A unified paradigm for thin film growth,” *Journal of Applied Physics* **93**, 278–285 (2002).
- ⁵⁷P. P. Dholabhai, E. Martinez, N. T. Brown, and B. P. Uberuaga, “On the mobility of carriers at semi-coherent oxide heterointerfaces,” *Physical Chemistry Chemical Physics* **19**, 23122–23130 (2017), wOS:000408671600052.
- ⁵⁸N. Schichtel, C. Korte, D. Hesse, and J. Janek, “Elastic strain at interfaces and its influence on ionic conductivity in nanoscaled solid electrolyte thin films—theoretical considerations and experimental studies,” *Physical Chemistry Chemical Physics* **11**, 3043–3048 (2009).
- ⁵⁹C. Korte, J. Keppner, A. Peters, N. Schichtel, H. Aydin, and J. Janek, “Coherency strain and its effect on ionic conductivity and diffusion in solid electrolytes – an improved model

for nanocrystalline thin films and a review of experimental data,” *Physical Chemistry Chemical Physics* **16**, 24575–24591 (2014).

⁶⁰J. A. Hirschfeld and H. Lustfeld, “First-principles study and modeling of strain-dependent ionic migration in ZrO₂,” *Physical Review B* **84**, 224308 (2011).

⁶¹S. Hull, “Superionics: Crystal structures and conduction processes,” *Reports on Progress in Physics* **67**, 1233 (2004).